PAPER • **OPEN ACCESS**

Thermal Transport in the Entry Region of a Microchannel in the Presence of Electro-osmotic Flow

To cite this article: Nicola Suzzi and Marco Lorenzini 2024 *J. Phys.: Conf. Ser.* **2893** 012088

Journal of Physics: Conference Series **2893** (2024) 012088 doi:10.1088/1742-6596/2893/1/012088

Thermal Transport in the Entry Region of a Microchannel in the Presence of Electro-osmotic Flow

Nicola Suzzi[1], **Marco Lorenzini**[2]

[1] Dipartimento Politecnico di Ingegneria e Architettura - Università di Udine - Via delle Scienze - 33100 - Udine (UD) - Italy
[2] Università di Bologna, DIN – Dipartimento di Ingegneria Industriale, Via Fontanelle 40, I-47121, Forlì (FC) Italy

E-mail: marco.lorenzini@unibo.it

Abstract. The motion of a polar fluid in microducts induced by an external electric field, known as electro-osmotic flow, enables fluid circulation without the need for mechanical devices. This feature makes it particularly appealing for the thermal management of electronic components, as microchannels with almost any cross-sectional shape can be easily integrated on the chips. Therefore, it is essential to evaluate how the channel's geometry influences heat transfer performance. This study investigates the thermal entry region and fully developed electro-osmotic flow in a microchannel with a rectangular cross-section and smoothed corners, with one adiabatic wall and uniform temperature elsewhere. The paper proposes correlations for the Poiseuille and Nusselt numbers, taking into account the aspect ratio and non-dimensional smoothing radius under fully developed thermal and hydrodynamic conditions, which can be valuable for practical design purposes. The study also emphasizes how Joule heating may lead to the reversal of heat flow and how the thermal entry length is linearly dependent on the logarithm of the non-dimensional Joule heating in thermally developing flow. Additionally, it demonstrates that smoothing the corners may increase the local Nusselt number over sharp corners, but it may also shorten the thermal entry length.

1. Introduction

Over the past two decades, microchannels have become a pivotal area of research due to their inherent compactness and the unique ability to leverage phenomena that emerge predominantly at microscales, [1, 2]. While a significant corpus of research dedicated to exploring fundamental aspects, [3–7], continues to evolve, Micro-Flow Devices (MFDs) have progressively been integrated into a wide array of applications, signalling a promising trend for future developments, [8–10]. Among the variety of MFDs, microchannel heat sinks stand out for their remarkable capability in dissipating high heat fluxes, rendering them particularly valuable for the thermal regulation of electronic components. However, one notable limitation pertains to the pressure drop due to friction observed across these devices, a feature that is heightened in the context of liquid mediums. An interesting mitigation strategy involves the principle of electro-osmosis —a phenomenon predominantly relevant at the microscale— which facilitates the movement of a liquid adjacent to a charged surface upon the application of an external electric field across the microchannel, [11]. Utilizing a polar fluid in conjunction with channel walls that

exhibit a net electrical charge leads to the formation of an inhomogeneous charge distribution within the fluid. The application of an external electric field on the mobile ion layer adjacent to the walls produces a fluidic motion, known as electro-osmotic flow (EOF). Devices based on EOF are distinguished by their lack of mechanical moving components, absence of noise or vibration, and no need for lubrication. The miniature volumetric requirements for liquid reservoirs —capable of being integrated directly onto chip surfaces— enhance the practicability of the EOF technology. Comparative studies have demonstrated that EOF can yield Nusselt numbers approximately 10% higher than those achieved with pressure-driven flow (PDF) under identical geometric constraints. However, an increase in the applied voltage across electrodes to a critical threshold may induce notable Joule heating, potentially impacting the system's thermal efficiency, [12]. Several challenges accompany the utilization of EOF, including the significant influence of chemical composition at the interface on velocity profiles —dramatically diverging from the patterns observed in pressure-driven flows. Additionally, Joule heating within the fluid can weaken or entirely negate its cooling capability, [11]. The exploration of electro-osmotic flows in microchannels, encompassing a diverse array of cross-sectional geometries ranging from traditional circular ducts and parallel plates, [13] to more unconventional shapes such as polygonal, elliptical, and triangular ducts, [14], alongside the operational dynamics of electro-osmotic pumps (EOPs), [12, 15, 16], has been extensive. Notably, some of these investigations have targeted the optimization of electronic cooling systems, [12, 17]. The proliferation of research on EOF in microchannels in recent years has comprehensively examined various aspects, with a notable focus on channel geometry —significantly propelled by advancements in micro-fabrication technology. Optimizing the cross-sectional geometry of channels has been demonstrated to enhance thermal performance, mitigate pressure losses, and reduce entropy production, particularly through the rounding of corner edges, [18]. Furthermore, investigation has expanded to encompass pressure-driven flows within microchannels, both with and without the inclusion of viscous dissipation, [19,20], as well as to EOFs under conditions of fully developed flow and constant heat flux and perimeter temperature, [21]. The application of these findings facilitates a thorough first-law analysis, employing performance evaluation criteria (PEC), [22]. One notably underexplored aspect in the treatment of laminar flows is the heat transfer within the thermal entry region of hydrodynamically fully developed flow, known as the Graetz problem. This work specifically addresses a microchannel characterized by smoothed corners and an adiabatic side, and examines the fluid circulation induced by electro-osmosis. The heating effects attributed to both the channel walls at uniform temperature and Joule heating are considered. In conducting an analysis of the thermal and fluid dynamic characteristics of EOF in the fully-developed regime, practical correlations to compute the Poiseuille and Nusselt numbers as functions of the channel's non-dimensional geometric characteristics —chiefly its aspect ratio (β) and the radius of curvature of its smoothed corners (γ)— are derived. Additionally, the solution of the Graetz problem enables the knowledge of the complete three-dimensional temperature field and the axial Nusselt number distribution. Considerations regarding the dependence of the Nusselt number on non-dimensional Joule heating and the radius of curvature are also presented. The overarching aim of this paper is to augment both the fundamental comprehension of electro-osmotic phenomena and practical insights pertinent to the optimization of devices such as heat sinks and micropumps.

2. Mathematical model

The geometric configuration presented in Fig. 1 will be further elaborated on in the following sections. To maintain conciseness, only the non-dimensional forms of the governing equations are provided below, and readers are directed to the nomenclature for explanations of the symbols used. A detailed discussion on the derivation of the governing equations can be found in [21, 23]. All equations are formulated for a Cartesian reference system, with the z coordinate aligned with

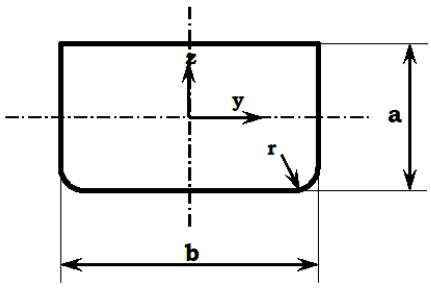

Figure 1: Sketch of the channel's cross section.

the flow direction, and the x and y coordinates corresponding to the cross-section as depicted in Fig. 1. The analysis necessitates solving the equations describing the distribution of electric potential, the velocity, and temperature fields, under the pertinent boundary conditions. The non-dimensional governing equation defining the electric potential distribution is therefore

$$\frac{\partial^2 \Psi}{\partial \mathrm{Y}^2} + \frac{\partial^2 \Psi}{\partial \mathrm{Z}^2} = \left(\mathrm{k_D\, D_h}\right)^2 \sinh \Psi \tag{1}$$

Accompanied by the boundary condition at the wall pertaining to the non-dimensional Stern potential.

$$\Psi|_{\partial\Omega} = \Psi_0 \tag{2}$$

The Debye-Hückel parameter, denoted as k_D, in Eq. (1), is linked to the thickness of the electric double layer and is computed at the temperature of the wall. Thus, variations in T_w (and T_i, since the temperature difference $T_w - T_i$ remains constant) define the range of variability for k_D for the scope of this investigation. The velocity profile is taken as fully developed, characterizing a laminar flow regime of a Newtonian, incompressible fluid, with thermophysical properties considered constant. The corresponding governing equation ia as follows:

$$\frac{\partial^2 \mathrm{U}}{\partial \mathrm{Y}^2} + \frac{\partial^2 \mathrm{U}}{\partial \mathrm{Z}^2} = \tilde{\mathrm{E}} \sinh \Psi \tag{3}$$

A no-slip condition at the fluid-wall interface, i.e., $\vec{U}(Y, Z) = 0$ is imposed. Knowledge of the velocity field $\vec{U}(Y, Z)$ enables the computation of the Poiseuille number, [24]. Subsequent to this, the energy equation furnishes the temperature distribution $\Theta(\mathrm{X}, \mathrm{Y}, \mathrm{Z})$:

$$\mathrm{Re\,Pr}\,\frac{U}{U_b}\,\frac{\partial \Theta}{\partial X} = \frac{\partial^2 \Theta}{\partial Y^2} + \frac{\partial^2 \Theta}{\partial Z^2} + Q \tag{4}$$

The parameter Q, positioned on the right-hand side in Eq. (4), represents the ratio of Joule heating to the heat transfer from the channel walls to the fluid:

$$\mathrm{Q} = \frac{\sigma\,\left(\mathrm{D_h\,E_x}\right)^2}{\lambda\,\left(\mathrm{T_w - T_i}\right)} \tag{5}$$

Pertaining to the energy equation, another condition is required in addition to those at the channel walls (uniform temperature along the heated perimeter and a zero heat flux at the adiabatic wall), explicitly the temperature profile at the inlet, which is assumed to be uniform. The non-dimensional boundary conditions are thus established:

$$\Theta|_{\partial\Omega} = 0,\ \nabla\Theta \cdot \hat{\mathrm{n}}|_{\partial\Omega-\Gamma} = 0,\ \Theta(\mathrm{Y}, \mathrm{Z})|_{\mathrm{X_0}} = 1 \tag{6}$$

Resolving the temperature field enables the local Nusselt number to be obtained according to Eq. (7):

$$\mathrm{Nu}(\mathrm{X}) = -\frac{\int_\Gamma \nabla\Theta|_\mathrm{X} \cdot \hat{\mathrm{n}}\mathrm{d}\Gamma}{\Gamma\Theta_\mathrm{b}(\mathrm{X})} \tag{7}$$

Wherein, in instances of complete thermal development of the flow, the expression simplifies to:

$$\mathrm{Nu}_\infty = -\frac{\mathrm{Q}\Omega}{\Gamma\Theta_\mathrm{b}|_{\mathrm{X}\to\infty}} \tag{8}$$

2.1. Method of numerical solution

The solution to the governing equations was derived using a proprietary computational code developed in `GNU Octave`, supported by additional libraries from `Octave Forge`, notably the `msh` package for generating unstructured meshes and the `bim` package, which accommodates the solving of diffusion-advection phenomena via both the finite volume and finite element methodologies. Within this context, the finite element approach was prioritized, leading to the assembly of discretized operators that yielded differential equations of the specified form:

$$-\nabla \cdot \left(\mathrm{C}_1 \nabla\Phi\right) + \mathrm{C}_2\Phi = \mathrm{C}_3 \tag{9}$$

Equation (1) is resolved across a two-dimensional domain that mirrors the cross-section, utilizing a refined mesh proximate to the boundaries to accommodate anticipated higher gradients. This is further streamlined to align with the framework of Eq. (9) through the linearisation of the right-hand side (pertaining to the reaction term) via a first-order Taylor polynomial. This process is iterated until convergence is achieved. The resultant value of Ψ is subsequently employed within Eq. (3) to obtain the velocity profile. Regarding the energy equation, its inherently parabolic nature permits the simplification of the three-dimensional Eq. (4) into a two-dimensional construct by implementing a q-weighted scheme:

$$\mathrm{Re}\,\mathrm{Pr}\,\frac{U}{U_b}\left[\frac{\Theta}{\Delta X}\right]^{n+1} - \theta\left[\frac{\partial^2\Theta}{\partial Y^2} + \frac{\partial^2\Theta}{\partial Z^2}\right]^{n+1} = \mathrm{Re}\,\mathrm{Pr}\,\frac{U}{U_b}\left[\frac{\Theta}{\Delta X}\right]^{n} + (1-\theta)\left[\frac{\partial^2\Theta}{\partial Y^2} + \frac{\partial^2\Theta}{\partial Z^2}\right]^{n} + Q \tag{10}$$

Where n denotes the integration step along the longitudinal axis of the channel (x-direction). The microchannel investigated has a reference length L and is characterised by its aspect ratio, $\beta \in [0,1]$, and non-dimensional radius of curvature, γ which has a maximum value dependent on the aspect ratio β according to $\max\{\gamma\} = 1/2\max\{1/2, \beta\}$. These two parameters determine the expression of the hydraulic diameter, which is also proportional to the reference (longer) side of the channel's cross section, a:

$$\mathrm{D_h} = \mathrm{a} \cdot \frac{2\beta - (\beta\gamma)^2(4-\pi)}{(1+\beta) - (\beta\gamma)(4-\pi)} \tag{11}$$

Computations exploit the problem's symmetry, along the vertical axis, so only half of the cross-section is computed, with a symmetry condition along Z=0:

$$\nabla\Psi \cdot \hat{\mathrm{n}} = 0 \;\; \nabla\mathrm{U} \cdot \hat{\mathrm{n}} = 0 \;\; \nabla\Theta \cdot \hat{\mathrm{n}} = 0 \tag{12}$$

Boundary conditions along the rest of the perimeter have already been mentioned while discussing the governing equations. As shown in [24], the addition of a so-called adiabatic preparation length, [24,25] is ininfluential, and is therefore omitted. Similarly, under the choices of water at $\mathrm{T_i} = 20\,^\circ\mathrm{C}$ as the base fluid, for $\mathrm{Q} \leq 10$, $20 < \mathrm{Pe} < 400$, so that axial conduction can be neglected too. The model has been tested for grid independence, taking the values of

the Poiseuille and Nusselt number as benchmark quantities, choosing a geometry with $\beta = 3/4$ and $\gamma = 1/2$ and values of $\kappa_D D_h = 9.77$ and $\Psi_0 = 9.78$ respectively. Computations were run for decreasing values of the grid spacing parameter l_c. It was found that a value of $l_c = 5 \cdot 10^{-3}$ ensures grid independency of the solution. The numerical model was verified against the numerical results presented in [22], in terms of Poiseuille and Nusselt numbers for the fully developed flow, obtaining a maximum discrepancy of +0.51 %. Verification with experimental results [12, 26] was also successfully carried out, as discussed at length in [23]; the results are reported in Fig. 2.

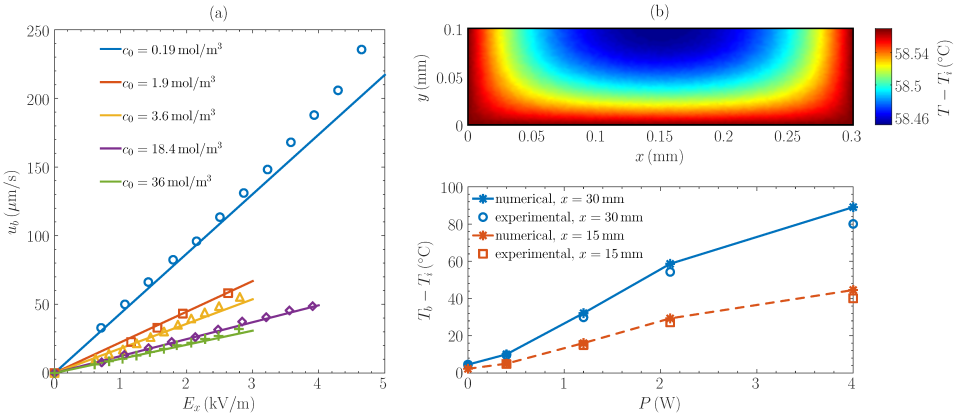

Figure 2: Computed bulk velocity (continuous lines) and experimental measurements (markers) of [26] at different borax concentration and electric field intensity, (a). Bulk temperature plot of numerical versus experimental [12] data as a function of thermal power at both middle and outlet cross-section of a microchannel (the computed, outlet temperature profile for a thermal power of 2.1W is also shown) (b).

3. Results and discussion

After thorough verification and validation, this study examined the fully-developed flow, encompassing both hydraulic and thermal development, within a microchannel. The objective was to ascertain the variations in the Poiseuille and Nusselt numbers, indicators of frictional losses and heat transfer capabilities, respectively. The analysis utilized deionized, ultrafiltered water as the polar fluid under examination, maintained at an inlet temperature $T_i = 20\,^\circ\mathrm{C}$. The numerical setup incorporated a Stern potential $\Psi = 0.1\,\mathrm{V}$ and an electric field along the z-direction $E_z = 10^6\,\mathrm{V \cdot m^{-1}}$, resulting in a Debye-Hückel parameter $\kappa_D D_h = 9.77$ and a non-dimensional wall potential $\Psi_0 = 9.78$. Moreover, the heated walls were constantly maintained at a temperature $T_w = 45\,^\circ\mathrm{C}$. It is critical to highlight that variations in the magnitude of the non-dimensional electric field $\tilde{E}$ and the value of Q bear no impact on the Poiseuille or Nusselt numbers, as the profiles of velocity and temperature remain invariant regardless of the Debye-Hückel parameter or $\tilde{E}$.

Figure 3 further presents an illustrative plot, showcasing the non-dimensional potential Ψ, velocity U, and temperature, Θ fields over the microchannel cross-section. The baseline geometry of the cross-section is rectangular, characterized by an aspect ratio β, which correlates the lengths of the two sides. Various configurations were analyzed, modifying the aspect ratios from a square cross-section ($\beta = 1$) to a considerably flatter duct ($\beta = 0.1$), at increments of 0.1, alongside a range of smoothing radii from sharp ($\gamma = 0$) to the maximum permissible for a given β ratio. An insightful finding from the analysis, as exemplified for $\beta = 0.6$ and $\gamma = 0.5$ in Fig. 3, reveals that smoother corners significantly enhance the transport of both momentum and energy compared

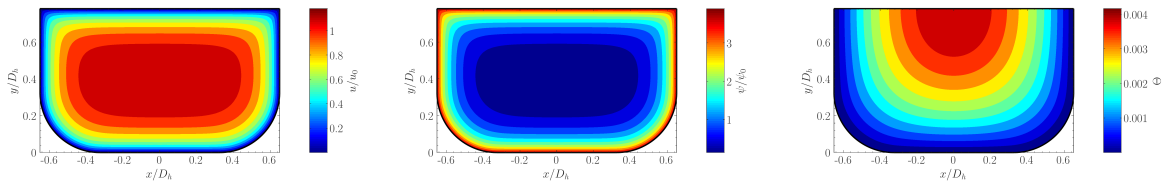

Figure 3: Non-dimensional potential (left), velocity (middle) and temperature (rigth) fields over the channel cross-section.

to the baseline sharp-cornered section. Attenuated gradients at the channel center, as opposed to the walls, account for almost flat potential and velocity profiles in the central area, with a marked variation near the walls. The temperature distribution notably peaks in the mid-section adjacent to the adiabatic wall, owing to Joule heating of the fluid.

The extensive investigation entailed 110 numerical runs, the outcomes of which are plotted in Fig. 4, correlating to the Poiseuille and Nusselt numbers, respectively. These figures effectively map the numbers as a function of the radius of curvature across ten different aspect ratios, encompassing the effects across an extensive range of geometries.

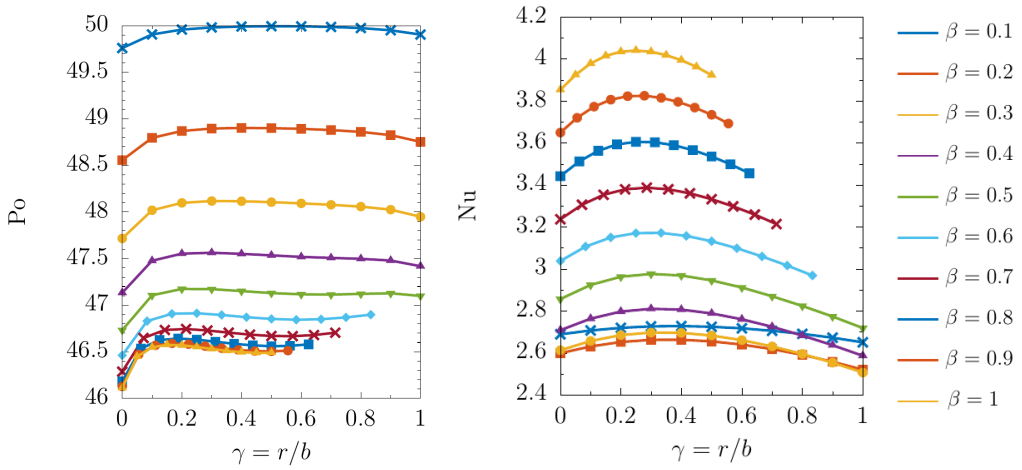

Figure 4: Poiseuille (left) and Nusselt (rigth) numbers as a function of γ for different aspect ratios.

The analysis highlighted a discernible trend within the Poiseuille numbers, illustrating an increment for all smoothed sections vis-à-vis the reference geometry with sharp corners. This trend manifested modest variations across the investigated spectrum. Notably, the lowest aspect ratio exhibited the highest Poiseuille number, underscoring a significant correlation between aspect ratio and frictional loss. Concurrently, the investigation into the Nusselt numbers unveiled more pronounced variations, with the maxima readily identifiable, conspicuously so for larger aspect ratios. A notable observation was that the Nusselt numbers at larger values of γ could potentially dip below those for $\gamma = 0$, emphasizing the nuanced influence of corner smoothing on heat transfer capabilities. Summarizing, this study has charted the impact of varying aspect ratios and radii of curvature on the Poiseuille and Nusselt numbers within a microchannel. The

data so obtained underpin the formulation of correlations for designing optimally performing microchannels. These correlations, expressed by Eqs. (13) and (14), coupled with the coefficients and the root mean square error delineated in Table 1 constitute a practical tool for enhancing microchannel design and performance.

$$\mathrm{Po} = a_{00} + \sum_{n=1}^{3} a_{n0}\,\beta^n + \sum_{n=1}^{3} a_{0n}\,\gamma^n + a_{11}\,a_{11}\,\beta\,\gamma + a_{12}\,\beta\,\gamma^2 + a_{21}\,\beta^2\,\gamma \tag{13}$$

$$\mathrm{Nu} = b_{00} + \sum_{n=1}^{3} b_{n0}\,\beta^n + \sum_{n=1}^{3} b_{0n}\,\gamma^n + b_{11}\,b_{11}\,\beta\,\gamma + b_{12}\,\beta\,\gamma^2 + b_{21}\,\beta^2\,\gamma \tag{14}$$

Table 1: Fitting coefficients of Eqs. (13) and (14) for the estimation of Nusselt number and Poiseuille number of a fully developed flow and Root Mean Square Error (bottom row).

Poiseuille number Eq. (13)		**Nusselt number Eq. (14)**	
a_{00}	+50.8162	b_{00}	+10.1790
a_{10}	-14.0158	b_{10}	-12.4539
a_{20}	+14.6258	b_{20}	+12.3036
a_{30}	-5.19479	b_{30}	-4.11363
a_{01}	+3.59595	b_{01}	+1.03360
a_{02}	-6.58458	b_{02}	-1.25171
a_{03}	+3.66162	b_{03}	+0.500750
a_{11}	+2.01872	b_{11}	+1.87850
a_{12}	-1.29980	b_{12}	-0.751240
a_{21}	-0.761764	b_{21}	-0.672452
$RMSE$	6.53×10^{-2}	$RMSE$	1.68×10^{-2}

3.1. Thermal entry length

The investigation of the thermal entry length, traditionally known as the Graetz problem, forms the focus of the succeeding analysis. This involves the resolution of Eqs. (1), (3) and (4) to determine $\mathrm{L_{th}}$. Illustratively, Fig. 5 delineates the three-dimensional thermal profile alongside the two-dimensional representation of the Nusselt number's cross-sectional distribution for parameters $\beta = 0.6$ and $\gamma = 0.5$.

In more detail, Fig. 5 presents a three-dimensional visual of the temperature field and the Nusselt number distribution in the flow direction. Successively, Fig. 6 plots the non-dimensional thermal entry length versus the ratio of Joule heating to heat transfer from the walls. Figure 7 shows the Nusselt number's dependency on the axial position for $\beta = 0.5$ with varying radius of curvature. The high value of Q juxtaposed with a relatively low electric field produces a comparatively short thermal entry length $\mathrm{L_{th}}$. This leads to the rapid attainment of fully developed conditions along the channel, which also make it useless for cooling purposes, as the local and, eventually, the overall temperature of the fluid is higher than that of the wall.

Several general observations can nonetheless be inferred:

1 Close to the channel entrance, the effects of Joule heating are ostensibly negligible; rather, convection and conduction dominate as the primary mechanisms of heat transfer.

2 The emergence of a vertical asymptote at $\mathrm{X} = 5.2$ signals a transition in the bulk temperature Θ_b, owing to the influence of Joule heating,

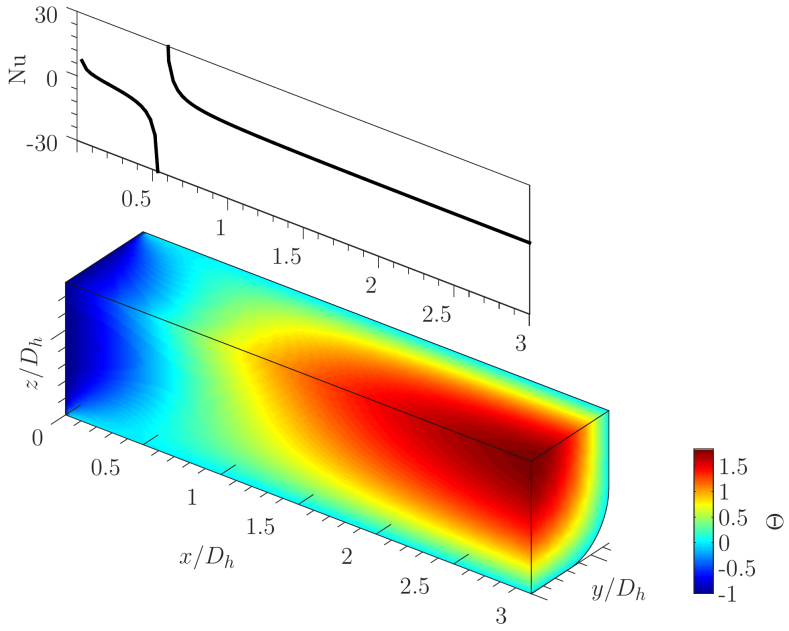

Figure 5: Three-dimensional temperature field and Nusselt number profile along the direction of flow.

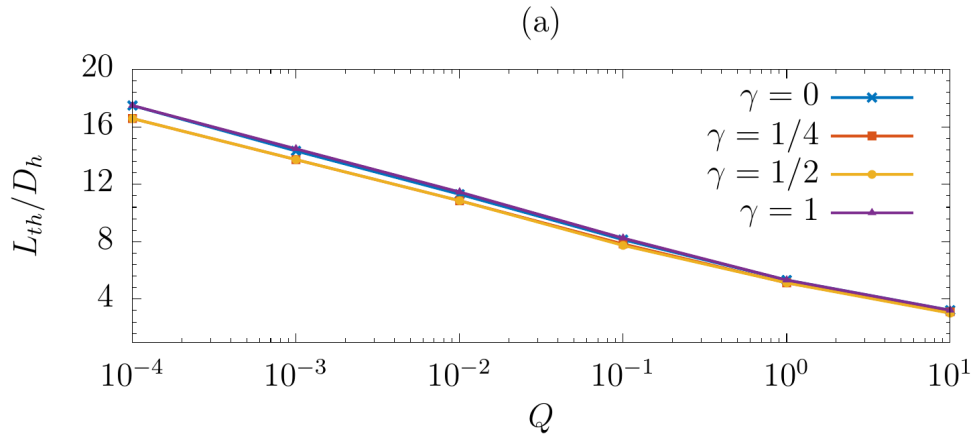

Figure 6: Non-dimensional thermal entry length as a function of the Joule heating to heat transfer ratio.

3 Post-asymptote, Joule heating impedes heat diffusion from the channel walls into the fluid.

4 The attainment of L_{th} occurs at X = 1.30

Acknowledging a shift in the heat transfer direction and understanding the extension of L_{th} are of practical importance. This is because the span of L_{th}, if significant within the channel, makes correlations for fully developed flow inapplicable. Further examination and implications are discussed in the context of Fig. 6, derived for $\beta = 0.5$, where the non-dimensional thermal

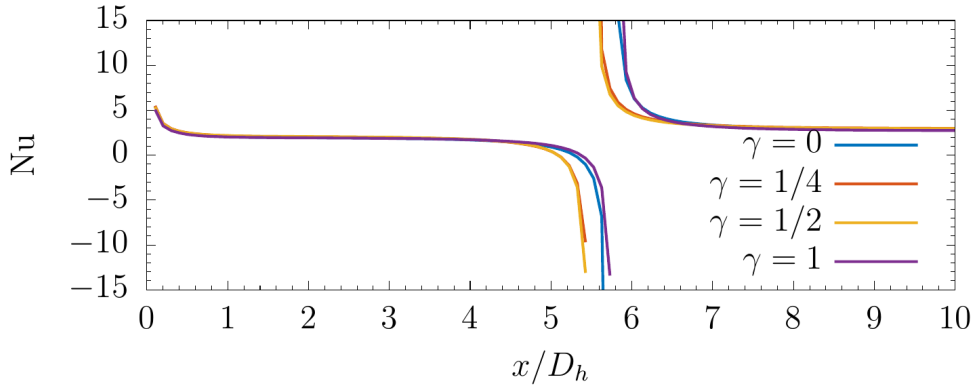

Figure 7: Nusselt number as a function of the axial position, for $\beta = 0.5$ and varying γ.

entry length's relationship with the logarithm of the non-dimensional Joule heating is explicated.

$$\frac{L_{th}}{D_h} \propto \log_{10}\left(\frac{1}{Q}\right) \tag{15}$$

Contrarily to observations made in [23] about channels with all sides heated, smoothing the channel corners does not uniformly result in a reduced thermal entry length. This assertion is corroborated by Fig. 7, formulated for the same aspect ratio. Here, the asymptote is encountered at shorter distances from the entry for intermediate radii of curvature compared to a channel with sharp corners. However, maximum smoothening ($\gamma = 1$) slightly advances the asymptote further than in channels with sharp corners.

4. Conclusions

The study has explored the effects of aspect ratio and corner radius curvature on Poiseuille and Nusselt numbers within a microchannel featuring one adiabatic wall, subject to electro-osmotic flow with appreciable Joule heating. The adherence to fully developed flow conditions facilitated the derivation of correlations for Po and Nu as a function of the aspect ratio and curvature radius. The analysis definitively indicates that corner smoothing enhances both frictional losses and heat transfer, with Nu(γ) showcasing a maximum dependent on β. Through solving the Graetz problem, the impacts of non-dimensional Joule heating and radius of curvature γ on both thermal entry length and Nusselt number distribution along the channel were elucidated. Such findings not only hold practical applicability but also augment the fundamental comprehension of the phenomena under study.

References

[1] Venkatesan S, Jerald J, Asokan P and Prabakaran R 2020 *Lecture Notes in Mechanical Engineering* 235–245
[2] Hossan M, Dutta D, Islam N and Dutta P 2018 *Electrophoresis* **39** 702–731
[3] Kuznetsov V 2019 *Heat Transfer Engineering* **40** 711–724
[4] Morini G L, Lorenzini M, Colin S and Geoffroy S 2006 Experimental investigation of the compressibility effects on the friction factor of gas flows in microtubes *Proceedings of the 4th International Conference on Nanochannels, Microchannels and Minichannels, ICNMM2006* vol 2006 A pp 411–418
[5] Yang Y, Chalabi H, Lorenzini M and Morini G 2014 *Heat Transfer Engineering* **35** 159–170
[6] Keepaiboon C, Dalkilic A, Mahian O, Ahn H, Wongwises S, Mondal P and Shadloo M 2020 *Physics of Fluids* **32**
[7] Lorenzini M, Daprá I and Scarpi G 2017 *Applied Thermal Engineering* **122** 118–125

[8] M Ohadi, K Choo, S Dessiatoun and E Cetegen E 2013 *Next Generation Microchannel Heat Exchangers* (New York, Heidelberg: Springer Briefs in Applied Sciences and Technology)
[9] Han Y, Liu Y, Li M and Huang J 2012 A review of development of micro-channel heat exchanger applied in air-conditioning system vol 14 pp 148–153
[10] Tuckerman D, Pease R, Guo Z, Hu J, Yildirim O, Deane G and Wood L 2011 Microchannel heat transfer: Early history, commercial applications, and emerging opportunities vol 2 pp 739–756
[11] Kirby B 2010 *Micro- and Nanoscale Fluid Mechanics* (Cambridge, UK: Cambridge University Press)
[12] Al-Rjoub M, Roy A, Ganguli S and Banerjee R 2011 *International Journal of Heat and Mass Transfer* **54** 4560–4569
[13] Mala G, Li D, Werner C, Jacobasch H J and Ning Y 1997 *International Journal of Heat and Fluid Flow* **18** 489–496
[14] Wang C Y and Chang C C 2011 *ELECTROPHORESIS* **32** 1268–1272
[15] Geri M, Lorenzini M and Morini G 2012 *International Journal of Thermal Sciences* **55** 114–121
[16] Morini G L, Lorenzini M, Salvigni S and Spiga M 2005 Thermal performance of silicon micro heat-sinks with electrokinetically- driven flows *Proceedings of the 3rd International Conference on Microchannels and Minichannels, 2005* vol PART B pp 231–236
[17] Pramod K and Sen A 2014 *Journal of Electronic Packaging, Transactions of the ASME* **136** 03101201–03201214
[18] Ray S and Misra D 2010 *International Journal of Thermal Sciences* **49** 1763–1775
[19] Lorenzini M and Morini G 2011 *Heat Transfer Engineering* **32** 1108–1116
[20] Lorenzini M and Suzzi N 2016 *Heat Transfer Engineering* **37** 1096–1104
[21] Lorenzini M 2020 *Thermal Science and Engineering Progress* **19**
[22] Webb R 1984 *Principles of Enhanced Heat Transfer* (New York: Wiley)
[23] Suzzi N and Lorenzini M 2021 *Fluids* **6**
[24] A Barletta and E Magyari 2006 *Int. Commun. Heat Mass* **33** 677–685
[25] Suzzi N and Lorenzini M 2019 *International Journal of Thermal Sciences* **145** 10603201–10603210
[26] Sadr R, Yoda M, Zheng Z and Conlisk A 2004 *Journal of Fluid Mechanics* **506** 357 – 367

Nomenclature

a	Longer side	m
A	Area	m^2
b	Shorter side	m
D	Diameter	m
e	Unit electron charge	C
E	Electric field component	$V \cdot m^{-1}$
$\tilde{E}$	Nondimensional electric field	-
k_B	Boltzmann Constant	$J{\cdot}K^{-1}$
k_D	Inverse of the Debye length	m^{-1}
$k_D \cdot D_h$	Debye–Hückel parameter	-
l_c	Grid spacing parameter	-
L	Channel length	m
L_{th}	Thermal entry length	m
Nu	Nusselt number	-
Pe	Peclet number	-
Pr	Prandtl number	-
Q	Quantity defined by Equation (5)	-
Re	Reynolds number	-
T	Temperature	K
u	Velocity component along the x-axis	$m{\cdot}s^{-1}$
U	Nondimensional velocity	-
x	Axial coordinate	m
X	Nondimensional x-coordinate	-
Y	Nondimensional y-coordinate	-
z_i	Ion valence	-
z	Nondimensional z-coordinate	-
Greek letters		
β	Aspect ratio of the channel	-
γ	Nondimensional smoothing radius	-
Γ	Cross-sectional heated perimeter (nondimensional)	-
$\partial\Omega$	Nondimensional perimeter	-
ϵ	Absolute permittivity	$F{\cdot}m^{-1}$
λ	thermal conductivity	$W{\cdot}m^{-1}{\cdot}K^{-1}$
Φ	Generic function −	
Ψ	nondimensional electric potential	-
Ψ_0	nondimensional Stern potential	-
σ	electric conductivity	$S{\cdot}m^{-1}$
Θ	Nondimensional temperature	K
ζ	Stern potential	V
Subscripts		
b	Bulk	
i	Inlet	
th	Thermal	
w	Wall	
x	Component along the x-direction	
∞	Fully developed	